Surface and Coatings Technology, v.381, 15 January 2020, 125142

Nano-Scale Residual Stress Depth Profiling in Cu/W Nano-Multilayers as a Function of Magnetron Sputtering Pressure

[1]León Romano-Brandt, [1]Enrico Salvati, [2]Eric Le Bourhis, [1]Thomas Moxham, [3]Igor P. Dolbnya and [1]Alexander M. Korsunsky

[1]Multi-Beam Laboratory for Engineering Microscopy, Department of Engineering Science, Parks Road, Oxford OX1 3PJ, UK

[2]Institut P', UPR 3346, CNRS - Université de Poitiers, France

[3]Diamond Light Source, Didcot, UK

Abstract

Residual stresses in thin films and multi-layered coatings fabricated by physical vapour deposition largely affect their mechanical and thermal reliability during operation in numerous fields of applications. By changing the argon working pressure in between each multilayer planar DC magnetron sputter deposition step, it is possible to control the residual stress distribution within coatings. A combination of FIB-DIC ring-core strain analysis, synchrotron XRD analysis based on the $\sin^2(\Psi)$ method and micro-cantilever deflection analysis is used to reconstruct the in-plane stress state of multilayer coatings at different deposition pressures, with a residual stress depth profile resolution of 50 nm. A clear transition from compressive to tensile residual stresses is observed with an increase of working pressure, with pronounced stress peaks near the substrate-coating interface. These peak stresses resolved by FIB-DIC ring-core analysis exceed the average XRD stress measurements significantly, thus providing a reasonable explanation for multilayer failure. Experimental results are presented and comprehensively discussed in the context of deposition conditions for different thin film applications.

Keywords

Residual Stress Depth Profile, Magnetron sputtering, FIB-DIC, Synchrotron XRD, Thin Films, Eigenstrain

1 Introduction

Nano-multilayers allow for the design of materials with unique mechanical, electrical, optical and functional properties by combining the advantages of different materials in a layered structure [1]. Copper and tungsten (Cu/W) multilayers are promising candidates for the thermal management at micro and nano scale, combining the excellent thermal and electrical conductivity of Cu with the low thermal expansion and high mechanical strength of tungsten [2–4].

Magnetron sputter deposition as one of the most popular Physical Vapour Deposition (PVD) methods includes a wide range process parameters, such as the argon working pressure, the target power and the substrate bias and temperature. These parameters can be used to fine-tune the stresses and the microstructure at the nanoscale during deposition [5]. Influencing factors have been systemically studied for decades [6], however, thicknesses used in technology have reduced significantly since then, away from several micrometre thick coatings towards the (sub-) nanometre scale, while the demands for thermal and mechanical reliability have increased. To bridge this gap, thorough knowledge of the relationship between deposition parameters and spatially resolved thin film properties are required. In the same time, analysis methods have improved significantly, allowing deeper insights into material property distributions as ever before.

Accurate estimations of residual stress are a key factor for their reliability design of nanostructured thin films and coatings [7]. Many applications, such as microelectronics, Micro Electromechanical Systems (MEMS), and sensors rely on the structural integrity of coatings, which are often only few nanometres thin. The arising complex stress field during energetic deposition, such as magnetron sputtering, is difficult to predict accurately, due to the number of interlinked mechanisms at atomic level involved [8]. Experimental measurements are therefore of crucial importance for understanding and designing the residual stress in thin films.

Recent advances in the resolution of combined Scanning Electron Microscopy (SEM) and Focused Ion Beam (FIB) devices have allowed for the development of new methods for the spatially resolved study of residual stresses at the nano scale [9]. Two main approaches have been presented recently: cantilever-based [10,11] and ring-core based [12,13]. The first type relies on deflection measurement of a coated cantilever, while removing individual material layers with the FIB and observing the change of deflection, allowing to calculate the stress state of the coating at a resolution of around 50 nm. The advantage of this method lies in the fact that no surface preparation is required, as the deflection is easily measurable. A clear disadvantage, however, is the fact that the cantilever is usually being milled on an edge of the sample, which requires sample cutting at the risk of stress field modifications. Sectioning the sample in preparation for cantilever milling thus carries the risk of disturbing the pre-existing stress field.

Ring-core based techniques rely on the creation of a stress-free material island by step-wise material removal [14]. During strain relief, frames are being acquired, which later allow for the reconstruction of the residual stress state. As this method requires a very high level of accuracy in surface point correlation via Digital Image Correlation (DIC), patterned surfaces need to be prepared for this method. One large advantage, however, is the possibility to probe the stress state at any location on the sample without altering the stress state. In addition, the milling times required are significantly lower as compared to micro-cantilevers, with a duration of around 20-40 minutes per measurement point, depending on the ring-core diameter. For this analysis, the ring-core depth profiling method was employed [14], which will be further explained in the following section. To confirm the FIB-DIC results, a micro-cantilever was milled in the centre of the sample and the deflection profile was extracted.

Finally, major advances regarding the availability, brilliance and focusing capability of Synchrotron light sources in the recent years have allowed to perform spatially resolved stress measurements of thin films and coatings by nano-diffraction. Albeit very complex sample preparation, this method permitted reliable insights into the residual stress state of coatings [15]. To confirm and expand the insights gained from the FIB-SEM methods, we employed classic wide-angle X-Ray diffraction for $\sin^2(\psi)$ analysis [8,16,17] to extract averaged residual stress magnitude present in the multilayer. The results presented in this article will be thoroughly discussed.

The residual stress variation during nucleation, grain boundary formation, single film growth and multi-layer deposition is complex and combines several mechanical effects. Understanding how the residual stress in nano-multi-layered systems arises during deposition at different working gas pressures therefore requires breaking the deposition process into smaller, mechanically meaningful intervals. In a first step, a single layer of tungsten is being deposited onto a Si substrate. Subsequently, the deposition is interrupted for a short period of time, after which a layer of copper is grown on the tungsten surface. This process is then being repeated for further nine bilayers of Cu/W. During these individual deposition steps, the residual stress within the coating changes significantly.

During nucleation and island growth on the substrate, the global average stresses are close to zero, due to the lack of a uniform film [8]. After the initiation of island coalescence, the residual stress becomes tensile, as the free surfaces convert into grain boundaries. During this process, it is of energetic advantage for the islands to accommodate internal tensile strains in order to form a uniform film and share grain boundaries with neighbouring islands [18]. As soon as the film has grown to a uniform layer, the effects of energetic particle bombardment begin to dominate the stress state. The phenomenon, known as ‘atomic peening’, affects the residual stress state significantly [19]. Highly energetic particles impacting the surface lead to recoil implantation of coating surface atoms and integration of argon atoms into the films. More specifically, the impact of particles on the surface also incorporates defects into the structure through displacement sequences within the grains [8]. The momentum propagation during magnetron sputter deposition can lead to both the motion of atoms to energetically favourable sites, such as vacancies, but also to the creation of point defects such as interstitials. These effects add up to a highly densified layer, which is stored mechanically as compressive residual stress.

Changing the in chamber pressure modifies the stress state significantly – a phenomenon that has been well-known for many years [6]. Several phenomena contribute to this effect: firstly, the larger quantity of Ar atoms in between the sputtering target and the sample surface result in a significantly lower mean free path length for the sputtered Cu and W atoms. The atomic peening effect is therefore reduced by a significant amount, as there is a larger momentum transfer between the working gas and the sputter material, resulting in a lower impact energy at the sample surface. This also leads to a reduced level of atomic implantation in between the grain boundaries. Finally, in addition to the lack of atomic peening and grain boundary implantation, a high working pressure inside the magnetron chamber leads to the tensile stress due to the formation of an under-dense columnar growth morphology, which is typical for refractory metals such as tungsten [8].

2 Material and methods

2.1 Multilayer deposition

Five multilayer systems were deposited onto naturally oxidized monocrystalline silicon (001), which were cleaned prior to deposition by acetone and ethanol rinsing, and dried under nitrogen flow. The working pressure (P) was varied from sample to sample using the following chamber pressures: P_1 = 0.50 Pa, P_2 = 0.66 Pa, P_3 = 0.74 Pa, P_4 = 0.81 Pa and P_5 = 0.89. Before deposition, the target was clean sputtered while the substrates were protected by a shutter. Each multilayer consists of ten bilayers of Cu/W 50/50 nm thin films were deposited at room temperature (RT) by planar magnetron sputtering in DC mode using Ar as working gas in a high vacuum system (base pressure ~$1 \cdot 10^{-5}$ Pa), resulting in a total film thickness of 1 μm. The sputtering rate was calibrated using X-ray reflectometry (XRR). Each of the W and Cu targets were 7.6 cm in diameter, with a purity 4N (i.e., 99.99%). The thin films were deposited at a constant target power of 130 W, using unbalanced magnetron, on grounded rotated substrates. The target-to-substrate distance was 18 cm.

2.2 FIB-DIC ring-core depth profiling

The FIB-DIC ring-core method is a well-established and thoroughly verified method for the semi-destructive probing of residual stresses at the micron scale. It is based on the gradual removal of material in a ring-core shape (Figure 1) with the intermediate acquisition of SEM frames at each milling steps. Mechanically disconnecting the central material 'island' from the surrounding strain field leads to a full elastic strain relief. This can be observed by tracking surface points of the central island using DIC in post-processing at an accuracy of around $\varepsilon \approx 10^{-5}$, which can then be used to back-calculate the average residual stresses present in the probed volume prior to milling, if the elastic properties of the material are known. Recent advances in this technique allow to extract the depth-dependant stress and strain profiles in milling direction, based on the FIB-DIC strain relief profiles and by employing the eigenstrain theory [20].

As the DIC requires a trackable surface pattern to correlate images from different milling steps without altering the residual stress state of the samples measurably, a 4.1 nm thin Au/Pd layer was deposited on top of the multilayers using a commercial sputter coater (SC7620, Quorum Technologies) at a sputtering rate of 0.092 nm·s^{-1}. A fixed target-to-sample distance of 45 mm was chosen, and the process current was adjusted to 18 mA. Subsequently, the surface was exposed to the FIB at a low beam current of 0.20 nA at 30 kV, creating a nanoscale surface speckle pattern [21] without affecting the multilayer beneath. This was confirmed by cross-sectional high-resolution SEM imaging. To confirm that the Au/Pd contrast layer did not alter the residual stress state in the multilayer systems, a 30 nm thin layer of Au/Pd was deposited on a 75 μm Kapton substrate, while the curvature was recorded *in situ*. The substrate did not show any change in curvature, confirming that the residual stress within the DIC contrast layer can be neglected for further analysis.

Subsequently, ring-cores of three different diameters were milled step-wise into the sample using FIB. The diameter of the ring-core was chosen according to the desired depth-sensitivity, as the sensitivity for strain reconstruction is limited to a depth-to-diameter ratio of h/d = 0.4. In the final analysis, a maximum of h/d = 0.25 was used. As a consequence, the chosen ring-core diameters for this analysis were D_1 =10 μm, D_2 = 5 μm and D_3 = 3 μm, and for each diameter three ring-cores were produced to minimise the statistical scatter of results (Figure 1). While D_3 returned the best depth resolution for the coating, D_1 probed further into the substrate and was used to analyse the interaction between substrate and

coating. D_2 as intermediate diameter improved the statics of both the coating and the upper part of the substrate. The FIB was operated at a beam energy of 30 keV and a beam current of 0.20 nA for the D_1 and D_2 ring-cores. For the D_3 ring-cores, however, a lower beam current of 0.04 nA was chosen to minimise the ion beam damage [22–25] of the smaller central island surface area. After each milling step, five SEM images were acquired for DIC analysis to improve the tracking statistics. As each ring-core affects the residual stress field due to local strain relaxation, the correct spacing needs to be chosen in between measurement points. It was shown that a distance in between ring-cores of five times the ring-core diameter is sufficient to avoid any mechanical interaction between points [9]. Therefore, the distance in between points corresponds to 5·D of the larger ring-core, respectively (Figure 1).

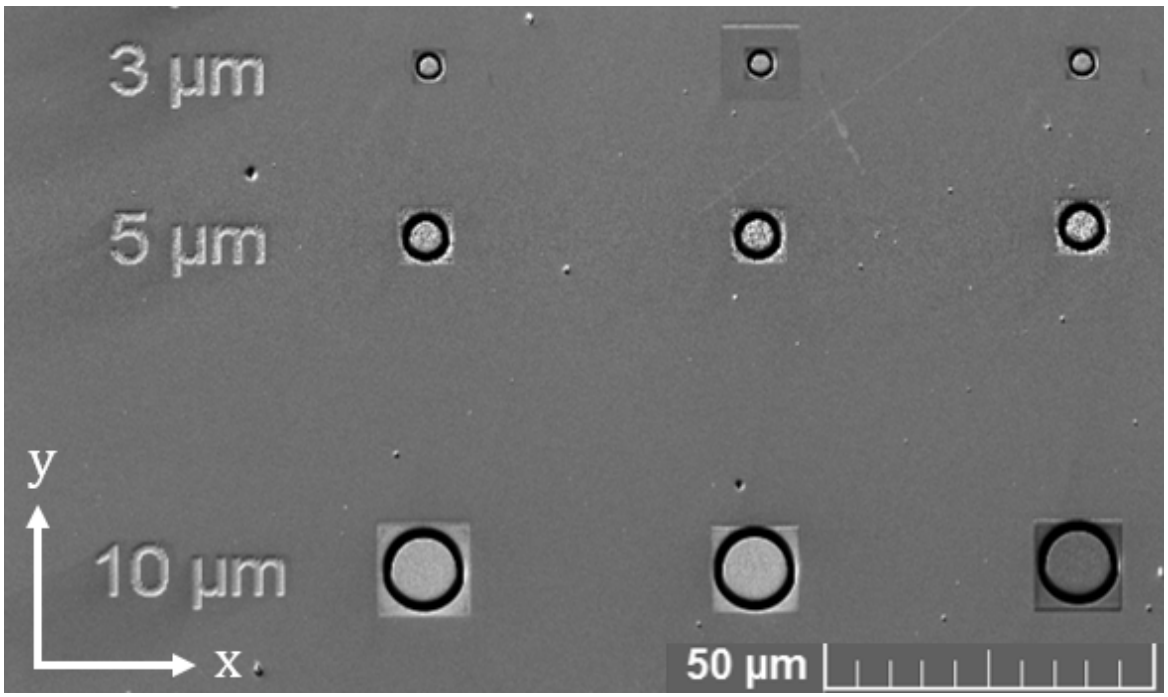

Figure 1. Arrangement of FIB markers for DIC depth-profiling analysis. Ring-core diameter indicated on the left.

2.3 Synchrotron XRD

To confirm the obtained FIB-DIC measurements, Wide-Angle X-Ray Scattering (WAXS) experiment was performed at the B16 beamline at Diamond Light Source (UK) in grazing angle scattering geometry. The chosen photon energy was 18 keV with a beam size of 250·250 μm^2, collimated by crossed slits, and a grazing angle of $\alpha = 1°$, resulting in a large interaction volume of the beam with the coating and therefore improved pattern statistics. The WAXS patterns were acquired for 360 s using an Image Star 9000 detector at a sample-detector distance of $66 \cdot 10^{-3}$ m, which was calibrated using a Lanthanum hexaboride (LaB_6) sample. The setup is shown in Figure 2.

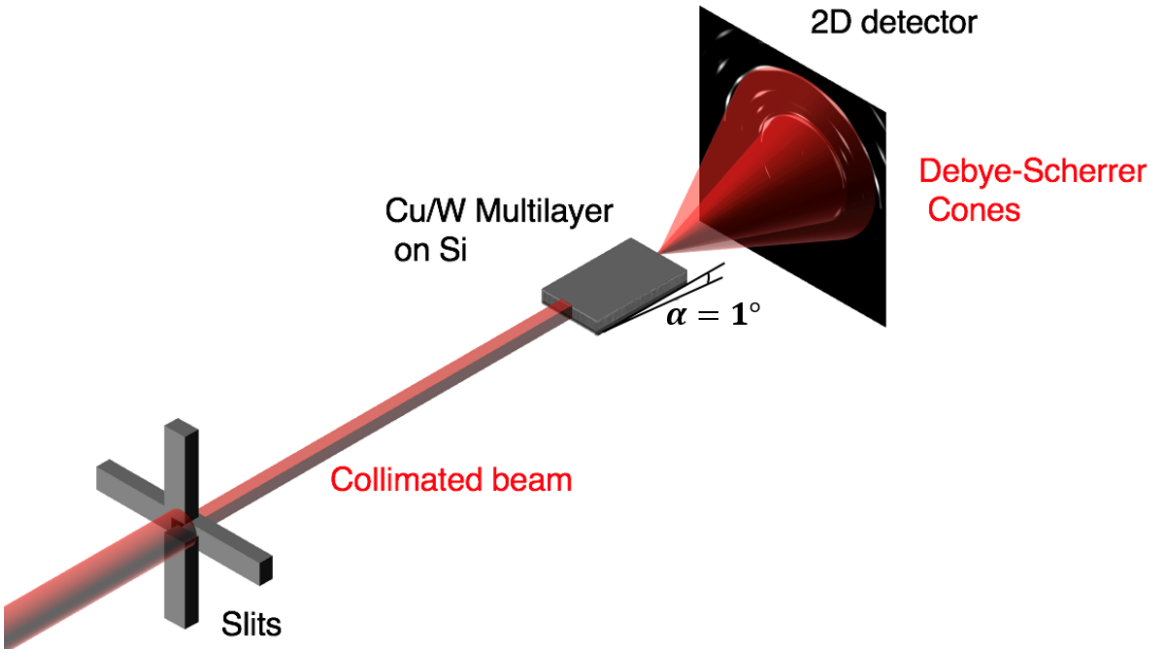

Figure 2. Synchrotron WAXS setup using collimated X-Ray beam and 2D area detector

The obtained WAXS diffraction patterns are shown in *Figure 3*, along with the identified phases and crystal orientations. Only the upper half of the Debye-Scherrer rings was used for further analysis, as the lower half was mostly absorbed by the substrate and did not contain any additional information for strain reconstruction due to the two-fold symmetry of powder diffraction rings.

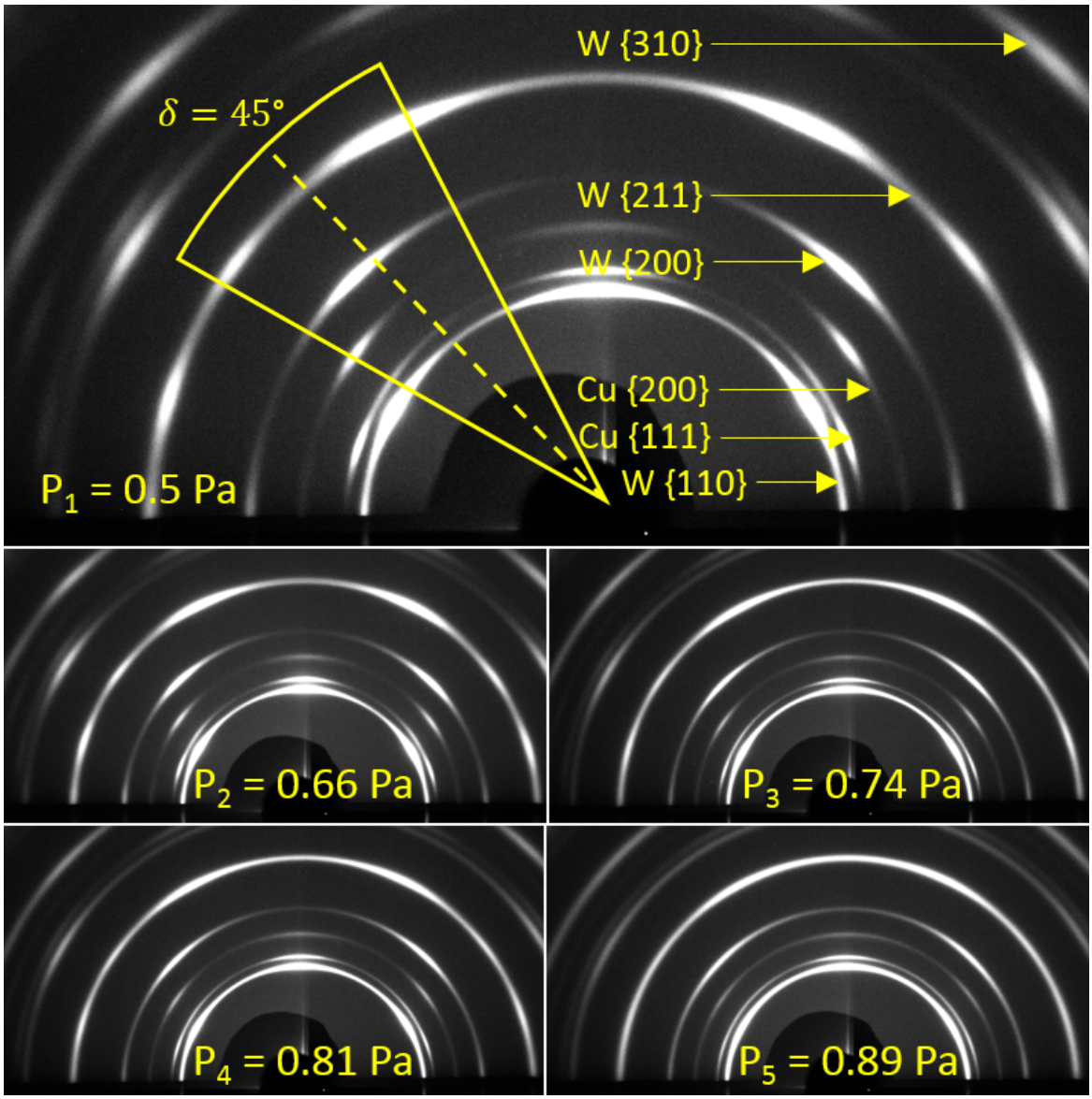

Figure 3. Synchrotron WAXS patterns of Cu/W 50/50 nano-multilayers deposited at different magnetron Ar working pressures. Crystal orientations are identified in the top figure.

2.4 Micro-Cantilever Deflection

To cross-check the measured residual stresses within the coating by a further independent method, a micro-cantilever was milled at the centre of the sample deposited at P_1 = 0.5 Pa, using the FIB at 30 keV energy and 0.2 nA beam current. In this way, it was ensured that the analysed stress field was undisturbed, as opposed to machining a micro-cantilever at a cut cross-section. One arising consequence, however, is the non-square shape of the cantilever cross-section caused by the inclined angle during milling, which needs to be accounted for an accurate residual stress reconstruction. Subsequently, SEM frames were acquired at an electron beam energy of 5 keV. Shape, dimensions and deflection of the cantilever are shown in Figure 4a, alongside the measurements extracted from the SEM frames shown in Figure 4b.

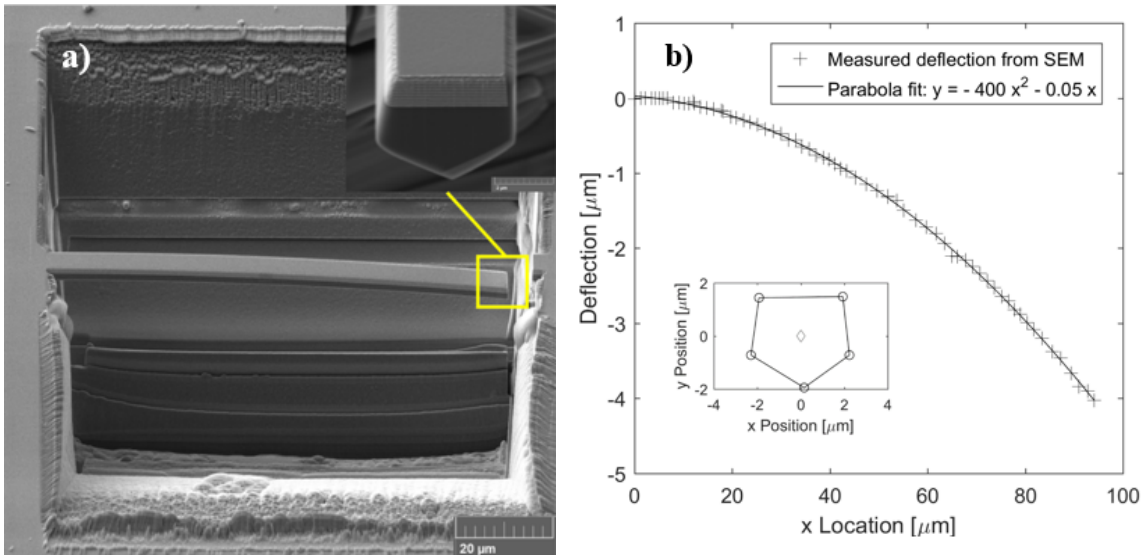

Figure 4a. Deflected micro-cantilever prepared by FIB milling. Top right corner: shape and dimensions of the cross-section, showing a clear contrast between Cu/W coating and Si substrate. Figure 4b. Deflection measured from SEM data, plotted alongside parabolic fit. Box: cross-section of cantilever from SEM frame.

3 Calculation

3.1 FIB-DIC micro-ring-core milling

To obtain full-field displacement and thus strain relief profiles, a MATLAB based DIC software was used to track surface points [26]. Subsequently, the strain relief profiles for the three measurement points of each ring-core diameter were averaged to a single profile. From this averaged strain relaxation profile, the residual elastic strain depth profile was reconstructed by following the approach described in [14]. The analysis was performed by analysing information provided by the strain relief curves lying within the normalised range $0.015<h/D<0.25$. Where h the milling depth and D is the ring-core diameter [14]. An example of strain relief profiles for the sample deposited at $P_5 = 0.89$ Pa is shown in Figure 5 for all three ring-core diameters against the FIB material removal depth, h. The 95% confidence interval shown as shaded area around the relaxation profile is determined by two error sources: 1) the uncertainty of the DIC process δ_{DIC}, which is determined by the tracking error of pixels which are smoothed by a Gaussian filter; 2) in order to extract the average strain relief taking place in the central ring-core island monitored by DIC, a first order polynomial is fitted to the displacement across the pillar diameter along the sought direction. The slope of this polynomial corresponds to the relaxation strain, leading to a slope fitting error δ_{fit}. These two errors are then combined by following the appropriate error summation rules.

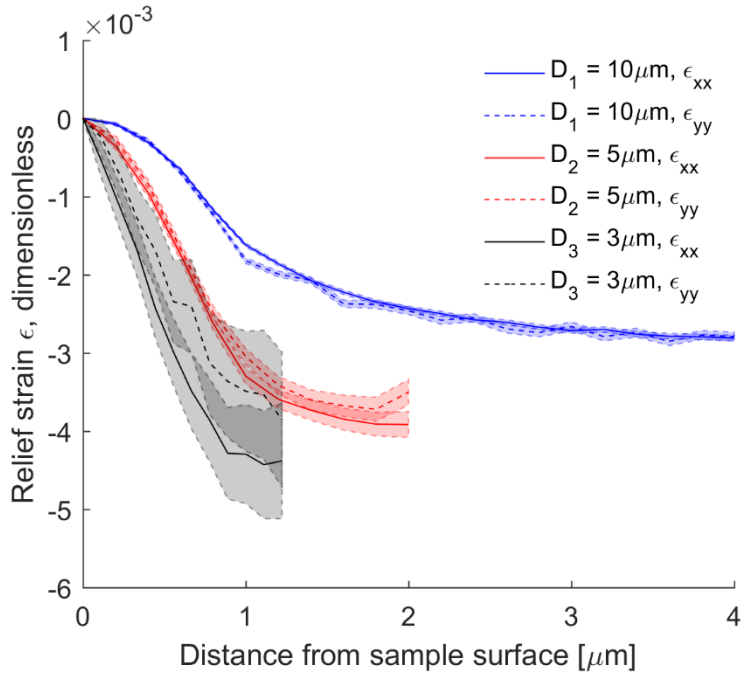

Figure 5. Relief strain for ring-cores of different diameters on the sample deposited at a magnetron working pressure of $P_1 = 0.89$ Pa. The shaded areas around the plot lines represent the 95% confidence interval.

Converting the obtained elastic strains to stresses [14] requires the Young's modulus E and Poisson's ratio ν, which were assumed to be 102 GPa and 0.34 for nano-crystalline Cu and 338 GPa and 0.36 for nano-crystalline W, respectively [1]. These properties were averaged by following the rule of mixture and considering a material ratio of Cu:W of 1:1, resulting

in average elastic properties of $\bar{E}_{Cu/W}$ = 220 GPa and $\bar{\nu}_{Cu/W}$ = 0.35. To calculate the stress within the substrate, a Young's Modulus of E_{Si} = 160 GPa and a Poisson's ratio of 0.27 were used [27], which explains the discontinuity of the residual stress profiles at a depth of 1 µm, caused by a change of elastic material properties used for calculation.

The resulting stress depth profiles are shown in Figure 6, which clearly reveal a transition in residual stress profiles from compression to tension with increasing magnetron chamber pressure during thin film deposition. The depth resolution of the shown stress graphs, which is directly linked to the milling step size, corresponds to the thickness of individual layers (50 nm). The 95% confidence boundaries resulting from averaging the probed stresses for several ring-core diameters and several measurement points per diameter are shown as shaded areas around the stress profiles. The larger error close to the multilayer surface can easily be explained by looking at the strain relaxation profiles in Figure 5. Smaller ring-core diameters increase the uncertainty significantly, due to their smaller DIC tracking surface area. As the smaller ring-core diameters probe the stresses closed to the surface, the error increases in this region.

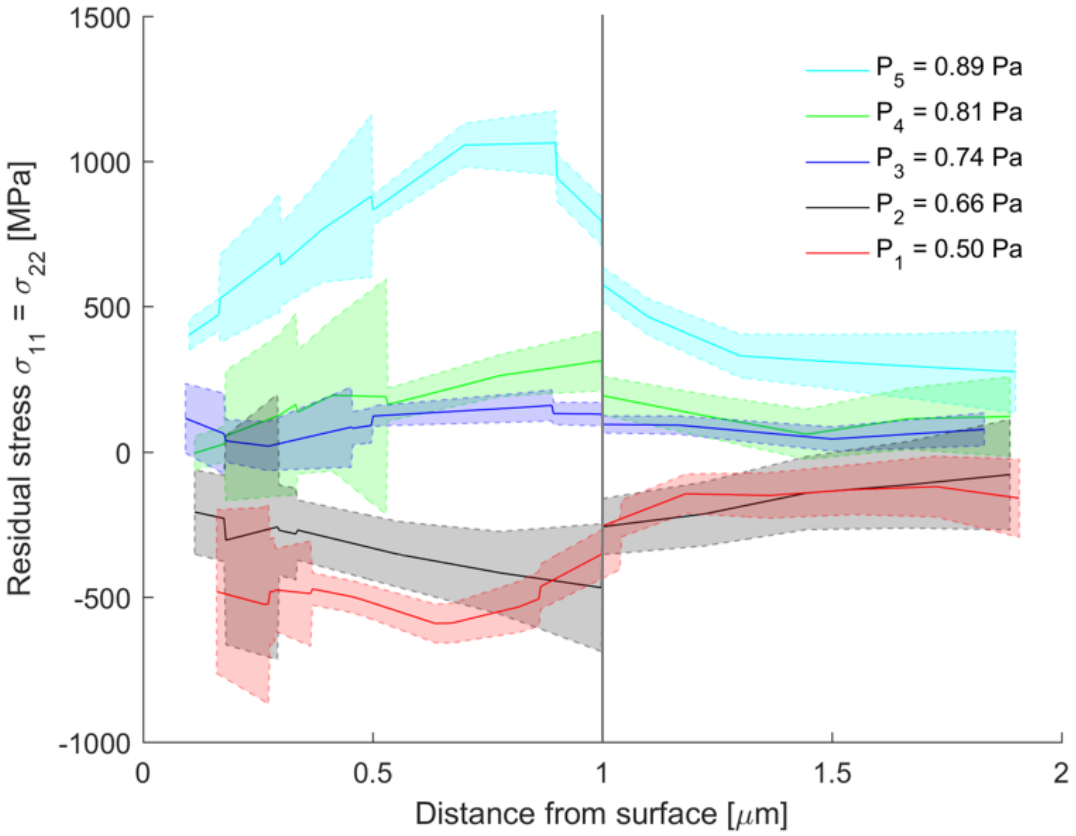

Figure 6. Residual stress depth profiles for different magnetron working pressures obtained from the FIB-DIC ring-core method. The shaded areas around the plot lines represent the 95% confidence interval.

3.2 Sin²(Ψ) analysis of XRD data

In order to extract the residual stress from the obtained WAXS patterns, the $\sin^2(\psi)$ technique was used. Having been developed in the early stages of experimental residual stress analysis, the $\sin^2(\Psi)$ technique is often being referred to as a method of reference to determine residual stresses [28,29]. As an experimentally easy and non-destructive near-

surface technique, it is mainly used to obtain averaged residual stress values, due to the comparably large beam size of laboratory X-Ray sources.

In contrast to the synchrotron XRD pattern acquisition chosen for this work, the traditional laboratory setup relies on a sample being illuminated with photons at an energy of around 8 keV. The obtained Bragg peaks are then collected by a point detector, resulting in a one-dimensional 2θ vs. intensity line profile. This traditional laboratory setup therefore requires tilting the sample around a line parallel to its surface (Ψ angle), to capture the stress induced lattice distortions can be observed by a shift in the measured 2θ peak position. The resulting $\sin^2(\Psi)$ vs. lattice parameter profiles can then be used to extract the average residual stress within the beam interaction volume.

A much faster way of capturing the $\sin^2(\Psi)$ behaviour involves the use of high energy WAXS with high photon flux, as presented in section 2.3. The use of area detectors with small pixel size and at short sample-detector distance allows to collect the full diffraction ring, as the 2θ range is narrowed down by the high photon energy. As the Debye-Scherrer cone angle approaches 90°, the scattering vector $\boldsymbol{k}_{\psi}$ is moving on a plane perpendicular to the laboratory coordinate system, which is approximately perpendicular to the sample surface at sufficiently small angle of incidence α. This scattering geometry results in a residual stress probing direction normal to the sample surface (Figure 7).

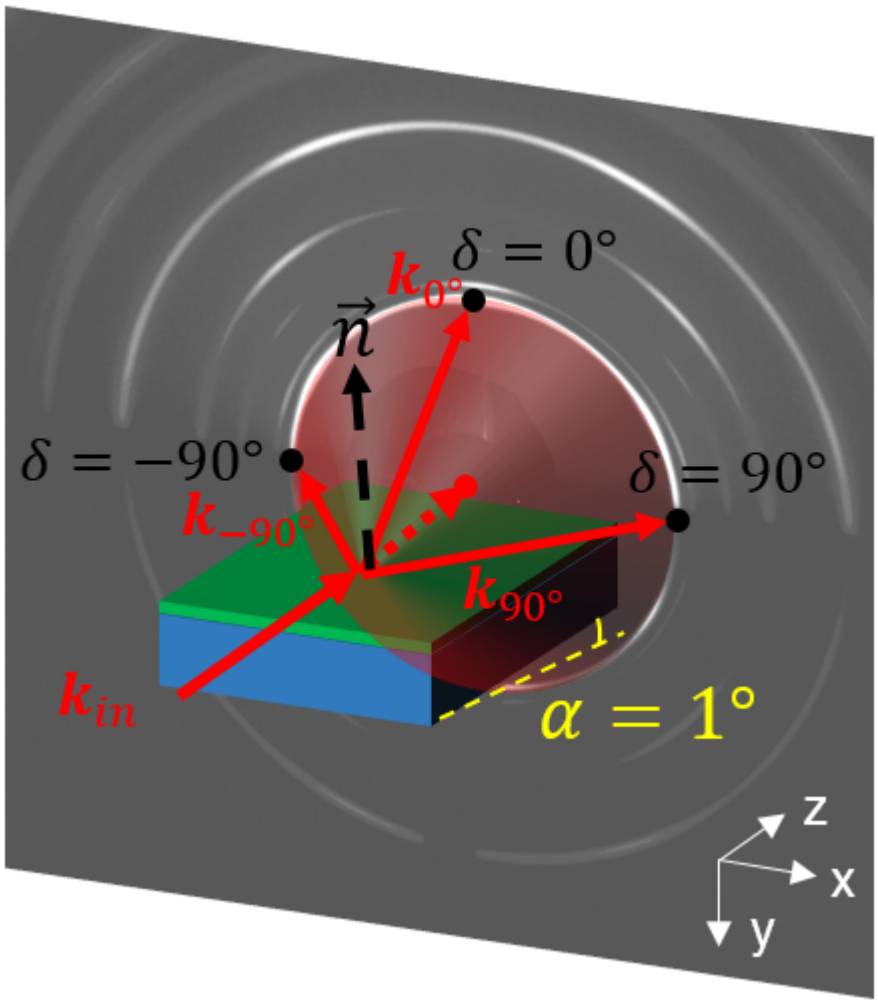

Figure 7. Diffraction geometry during synchrotron WAXS acquisition. Red: incoming and diffracted wave vectors $\mathbf{k}_{in}$ *and* $\mathbf{k}_{\delta}$*. Beamline coordinate system in white.*

To extract the $\sin^2(\Psi)$ behaviour of the coating, the obtained patterns were integrated by azimuthal binning in 22.5° steps, starting from the central $\delta = 0°$ position up to $\delta \lesssim \pm 90°$, resulting in a total number of nine measurement points. The comparably large step size for integration was chosen due non-uniform patterns caused by texture. Fit2D was used for integration, after an initial calibration using the acquired LaB6 diffraction pattern. High accuracy distortion correction was performed based on the calibration pattern prior to the experimental data analysis, ensuring the exclusion of spurious results. Four fully available Debye-Scherrer rings (Figure 3) were selected for azimuthal integration: W{110}, Cu{111}, Cu{200} and W{200}, of which all showed a linear $\varepsilon_{\Psi\phi}^{hkl}(\sin^2(\Psi))$ profile.

To calculate the angle Ψ based on the azimuthal angle δ, the following relationship was employed [16]:

$$\cos(\Psi) = \sin(\alpha)\sin(\theta) + \cos(\alpha)\cos(\theta)\cos(\delta) \tag{1.1}$$

Depending on the residual stress state within the diffracting material volume, the $\varepsilon_{\Psi\phi}^{hkl}(\sin^2(\Psi))$ behaviour can adopt different shapes [30]. To determine the residual stress state with the highest accuracy, the following relation based on an elliptical stress-strain relationship were adopted [31]:

$$\begin{aligned}\varepsilon_{\phi\Psi} = \frac{d_{\phi\Psi} - d_0}{d_0} &= \frac{1+\nu}{E}\{\sigma_{11}\,cos^2(\phi) + \sigma_{12}\,sin(2\phi) + \sigma_{22}\,sin^2(\phi) \\ &- \sigma_{33}\}\,sin^2(\Psi) + \frac{1}{E}\{\sigma_{33} - \nu\sigma_{11} - \nu\sigma_{22}\} \\ &+ \frac{1+\nu}{E}\{\sigma_{13}\,cos(\phi) + \sigma_{23}\,sin(\phi)\}\,sin(2\Psi)\end{aligned} \tag{1.2}$$

The angle ϕ refers to the rotation of the sample around the global y-axis (Figure 7). The same elastic properties E and ν were used as shown above for the FIB-DIC depth profiling analysis. Further justification for this assumption despite stronger texture at lower deposition pressure will be provided later, based on the ratio of σ_{Cu} to σ_W. The reference lattice parameter d_0 was set to be the d-spacing at $\delta = 0$, which will be justified at a later point.

Based on the origin of residual stresses within nanometric multilayers through island growth and grain boundary atom implantation, we can assume an equi-biaxial residual stress field in the surface plane direction of the sample. This simplifies the problem by assuming that $\phi = 0, \sigma_{11} = \sigma_{22}$, which yields

$$\begin{aligned}\varepsilon_\Psi = \frac{d_\Psi - d_{\Psi=0}}{d_{\Psi=0}} &= \frac{1+\nu}{E}\{\sigma_{11} - \sigma_{33}\}\,sin^2(\Psi) + \frac{1}{E}\{\sigma_{33} - 2\nu\sigma_{11}\} \\ &+ \frac{1+\nu}{E}\sigma_{13}\,sin(2\Psi).\end{aligned} \tag{1.3}$$

This can be rewritten as:

$$\varepsilon_\Psi = \frac{d_\Psi - d_{\Psi=0}}{d_{\Psi=0}} = \boldsymbol{A} + \boldsymbol{B}\,sin^2(\Psi) + \boldsymbol{C}\,sin(2\Psi),$$
$$\boldsymbol{A} = \frac{1}{E}\{\sigma_{33} - 2\nu\sigma_{11}\}, \boldsymbol{B} = \frac{1+\nu}{E}\{\sigma_{11} - \sigma_{33}\}, \boldsymbol{C} = \frac{1+\nu}{E}\sigma_{13}. \quad (1.4)$$

It can easily be seen that the only component showing a measurable sensitivity towards a change in $d_{\Psi=0}$ is the ellipse intercept with the y-axis **A**. For the further analysis, only the parameters **B** and **C** will be used, as they show no significant sensitivity towards a change in d_0. It is therefore possible to determine the composite residual stress $\{\sigma_{11} - \sigma_{33}\}$ and the shear stress σ_{13} without accurate estimation of d_0.

The out-of-plane stress (σ_{33}) and shear stress (σ_{13}) components were found to be negligible compared to the in-plane component. The calculated linear fits representing $\varepsilon_\Psi = \boldsymbol{B}\sin^2\Psi$ are thus shown in Figure 8 alongside the experimental data. The presented data shows the evolution of the $\sin^2(\Psi)$ behaviour depending on different magnetron chamber deposition pressures. The data error bars indicate the 95% confidence intervals for the Gaussian fitting of the diffraction peaks, based on the following error calculation for strain:

$$\delta_{\varepsilon\Psi} = \varepsilon_\Psi \cdot \sqrt{\left(\frac{\sqrt{(\delta_{d\Psi})^2 + (\delta_{d\Psi=0})^2}}{d\Psi - d\Psi=0}\right)^2 + \left(\frac{\delta_{d\Psi=0}}{d\Psi=0}\right)^2} \quad (1.5)$$

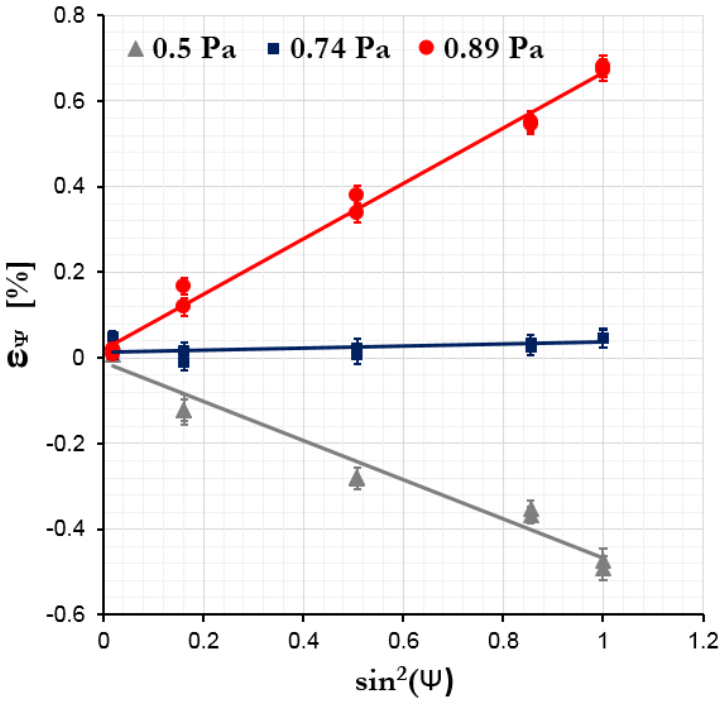

Figure 8. $\mathrm{Sin}^2(\psi)$ *profiles of the W{110} reflection after deposition at three different magnetron chamber pressures. Points: experimental WAXS data. Dashed line: fitted line profiles.*

The so obtained in-plane stress value ($\sigma_{11} - \sigma_{13}$) are shown in Figure 9 and Figure 10, respectively. The data clearly indicates significantly higher magnitudes of residual stresses within W as compared to Cu. As this behaviour is clearly indicating a strong dominance of isotropic W on the averaged residual stress, considerations regarding the orientation-dependence of the elastic properties of Cu would not affect the final averaged measurably. Further confirmation for this simplification can be drawn from the excellent agreement of experimental data between FIB-DIC and XRD analyses, as shown on Figure 10. Figure 9 shows a residual stress variation in W from $\sigma_{11} - \sigma_{33} = -1 \pm 0.46$ GPa at 0.5 Pa deposition chamber pressure to 0.87 ± 0.24 GPa at 0.89 Pa chamber pressure.

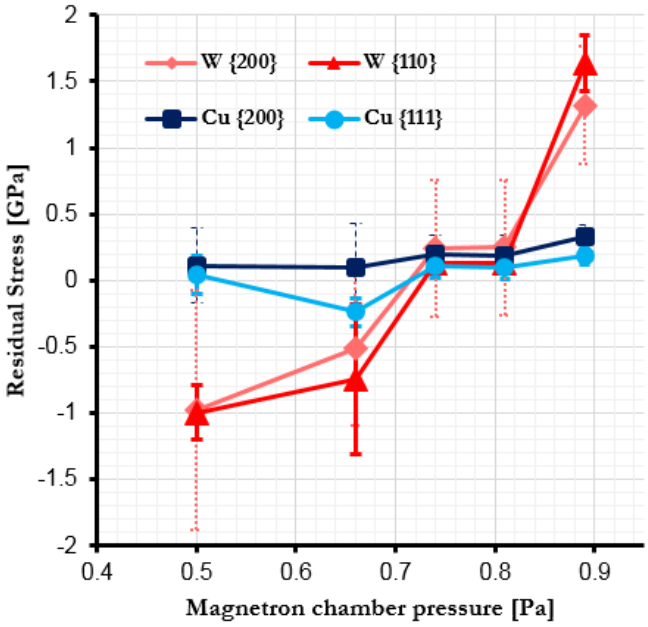

Figure 9. Residual stresses σ_{11}, based on ellipse fitting parameter B for individual W and Cu grain orientations..

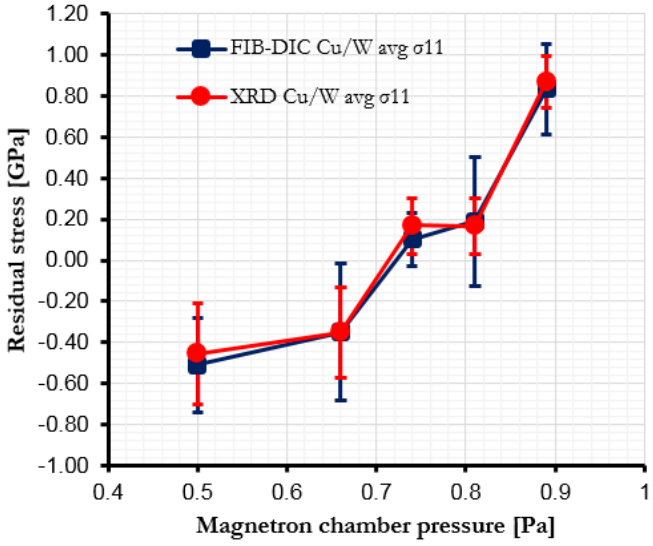

Figure 10. Comparison of residual stresses obtained from FIB-DIC and XRD measurements.

3.3 Micro-cantilever deflection

In order to compare the measured FIB-DIC with the deflection of a micro-cantilever, a forward calculation approach was chosen, following the eigenstrain deflection model of Korsunsky et al. [32]. A micro-cantilever was modelled to contain the residual stress profile obtained from FIB-DIC analysis, while assuming a linear variation of residual stress within the substrate down to a depth of 3.38 µm, corresponding to the total thickness of the micro-cantilever. Based on this residual stress profile and the cross-sectional geometry obtained from the real micro-cantilever, a curvature was predicted. To describe the residual stress within the cantilever, the following formulation was chosen:

$$\sigma(y) = E^*(y) \cdot (a + b \cdot y) - E^*(y) \cdot \varepsilon^*(y), \tag{2.1}$$

in which y is the coordinate pointing from the coating surface downwards, $E^*(y)$ is Young's modulus depending on y, b is the curvature of the cantilever deflection, $\varepsilon^*(y)$ is the eigenstrain profile as a function of depth and a refers to the component of strain that is uniform across the section and corresponds to the compressive deformation of the cantilever [32]. Equilibrium conditions lead to the following relationships for resultant force and moment, using a beam width function w(y):

$$F = \int \sigma(y) \cdot w(y)\, dy = 0 \tag{2.2}$$

$$M = \int \sigma(y) \cdot w(y) \cdot y\, dy = 0 \tag{2.3}$$

In the final step, the predicted curvature was compared to the one measured from the real micro-cantilever. Using the eigenstrain profile $\varepsilon^*(y)$ obtained from FIB-DIC returned a predicted curvature of -754±56 m^{-1}. This result is in excellent agreement with the experimental data presented in 2.4, which shows a curvature of -800±18 m^{-1}, resulting in a relative difference of only ~6%. Detailed calculations are presented in Appendix 7.1.

4 Results

The high spatial resolution of the FIB-DIC and eigenstrain nanoscale depth profiling method allowed to reveal the details of the stress variation within Cu/W nano-multilayers, as well as the stress-affected zone within the substrate.

The residual stress profiles clearly indicate the location of the stress peak at around $0.75 \cdot t_c$ distance from the sample surface, with t_c being the thickness of the multilayer coating. While approaching zero stress towards the sample surface, the stress peak magnitude can lie significantly above the average stress measured by XRD, as shown by graph P_1 in Figure 6 - an information which is particularly useful for the mechanical design of coatings. A clear correlation between the argon working pressure and the multilayer stress was made, showing a transition from compressive residual stresses at low working pressures to tensile residual stresses at higher pressures. It should be noted that not only the average stress value magnitude increases for low/ high working pressures, but also the difference between the peak stress and the average stress, making it highly important to consider the detailed stress profiles for reliability design under these deposition conditions.

Further insights include the stress transfer from coating to substrate. Starting from the substrate-coating interface, the residual stress asymptotically approaches the stress-free state at a depth of around 3 μm, which can be determined from extrapolation. Even though the performed XRD analysis can only provide averaged stress levels, it adds a significant amount of insights to this analysis, as the residual stress obtained by XRD and $\sin^2(\Psi)$ can be calculated for Cu and W separately.

Micro-cantilever deflection measurements confirmed the residual stress level determined by FIB-DIC analysis and hence supported the calculations based on a combination of FIB-DIC and XRD analysis. The agreement between FIB-DIC and micro-cantilever measurements was excellent, with a difference of around 6%.

5 Discussion

The residual stress state of thin films changes continuously during the magnetron sputter deposition: from tensile residual stresses during island coalescence to compressive residual stresses at low working pressures due to intergranular atomic implantation and atomic peening effects. As reflected in the residual stress profiles presented in Figure 6, it is easily possible to modify the residual stress state by changing the working Ar pressure inside the magnetron chamber. The presented data supports previous models [6,8], which suggest that a reduction in mean free path length of sputtering atoms reduces the atomic peening effect and additionally leads to the formation of an under-dense columnar growth morphology.

A hierarchical analysis of stresses has been proposed using three different independent and complementary techniques: firstly, XRD allowed assessing both Cu and W average through-thickness residual stress magnitudes. By using exclusively $\sin^2(\Psi)$ ellipse fitting parameters which were independent of the stress-free lattice parameter d_0, a robust analysis method was developed and employed. Consequently, detailed insights into the strain accommodation mechanisms within different materials and grain orientations were obtained (Figure 10).

Further to the above, the use of FIB-DIC ring-core milling permitted to study the stress accommodation within the coating multilayer-substrate systems spatially resolved at a high resolution of around 50 nm. Significant stress peaks became apparent, especially for the samples deposited at P = 0.89 Pa (Figure 6), suggesting that under-dense columnar growth in combination with a reduction of atomic peening significantly increases the difference between average and peak stress within the coating. In addition, the residual stress profiles showed that peak stresses occur in proximity to the substrate-coating interface, which facilitates mechanical failures at the substrate-coating interface. A discontinuity in the mechanical properties across this interface might promote mechanical failure further.

Finally, the deflection of a micro-cantilever was predicted, based on the residual strain relief profiles obtained from FIB-DIC, which matched the experimentally determined cantilever curvature with high accuracy. The proposed way of calculation takes into account the fact that the actual cantilever cross-section was not rectangular in the centre of the sample due to geometric constrains during ion beam milling. This technique turned out to be an ideal tool for the confirmation of experimental results obtained by novel experimental techniques.

If chosen carefully, residual stress becomes an additional degree of freedom available during engineering design process, not only by changing structural integrity properties but also functional ones. For instance, compressive residual stress in coatings can improve the tensile properties due to a pre-straining of the material. Not only the sign and magnitude of residual stress is important, but also gradients of residual stress can play an important role in modifying the final product's properties. For example, a uniform stress distribution is usually preferred, in order to avoid stress localisations within the coating, which may result in failure below the expected level of loading. In this respect, using the lowest possible working argon pressure to create compressive residual stress would not be the best solution from the structural point of view, as a compressive peak is deposited in near-substrate region which might give rise to failure. Instead, choosing a slightly higher pressure might help the reliability of the coating by creating a uniform residual stress distribution. If used in thermal applications, however, tensile residual stresses can be of advantage, as they may avoid buckling upon thermal expansion, if the coating has a higher thermal expansion coefficient than the substrate. Again, choosing the highest average residual stress could be detrimental, considering the tensile peak in the near substrate region. These examples show clearly the importance of the knowledge of stress profiles at

high resolution as compared to average stress values which can easily be extracted from X-Ray diffraction patterns.

6 Conclusions

High resolution depth profiles, as provided by the FIB-DIC analysis, revealed for the first time, how deposition conditions influence the stress distribution within nano-structured Cu/W coatings. While previous studies were only able to observe average stresses, it has become clear that these averages can significantly underestimate the confined peak stresses. Therefore, relying on averaged data from XRD for stress design and reliability considerations might lead to unexpected failure at locations of peak stress through mechanisms such as interfacial slip, void formation and crack propagation. The data obtained from the FIB-DIC depth profiling technique was cross-correlated with traditional synchrotron XRD methods and showed a high level of agreement.

7 Conflict of interest

There are no conflicts to declare.

8 Acknowledgements

Diamond Light Source is acknowledged for providing the beam time allocation under experiment MT19192-1.

9 Appendix

9.1 Cantilever deflection

To calculate the cantilever curvature based on the eigenstrain profile provided by FIB-DIC analysis, the following Young's modulus profile was used, based on the material properties introduces in 3.1. The profile is shown in Figure 12.

$$E^*(y) = \begin{cases} 220\ GPa, y \leq 1\mu m \\ 160\ GPa, y > 1\mu m \end{cases} \quad (3.1)$$

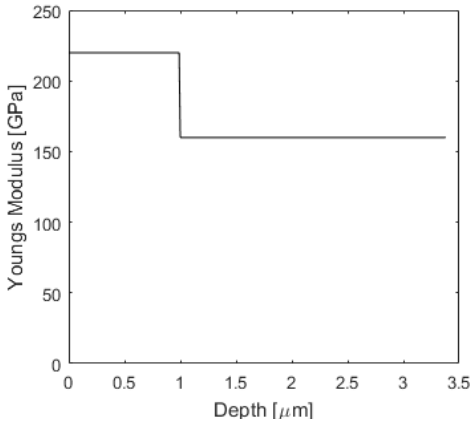

Figure 11. Distribution of the Young's modulus vs. depth used for predicting the cantilever deflection.

The eigenstrain profile $\varepsilon^*(y)$ obtained from DIC analysis was approximated using a fourth order polynomial and by assuming a drop in eigenstrain to zero at a depth of 3.38 µm, which corresponds to the total thickness of the micro-cantilever. The resulting eigenstrain function is given by

$$\varepsilon^*(y) = p_1 \cdot x^4 + p_2 \cdot x^3 + p_3 \cdot x^2 + p_4 \cdot x + p_5, \quad (3.1)$$

$$p_1 = -2.77 \cdot 10^{20}, p_2 = 1.92 \cdot 10^{15}, p_3 = -4.21 \cdot 10^{9}, p_4 = 2348, p_5 = 0.001731,$$

and shown in Figure 13.

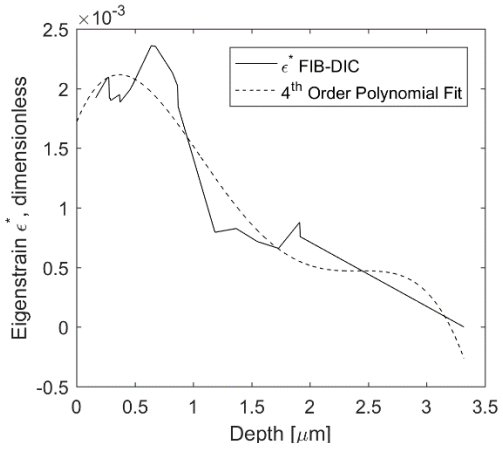

Figure 12. Eigenstrain profile obtained from FIB-DIC, extrapolated to a depth of 3.38 µm for predicting the cantilever curvature and presented alongside the 4th order polynomial fit.

To represent the geometry of the cantilever cross-section , the following dependence of width vs. depth was determined, which is shown in Figure 14:

$$w(y) = \begin{cases} 3.852 \cdot 10^{-6} + 0.3122 \cdot y, y \leq 2.162\ \mu m \\ 12.5626 \cdot 10^{-6} - 3.7162 \cdot y, y > 2.162\ \mu m \end{cases} \quad (3.2)$$

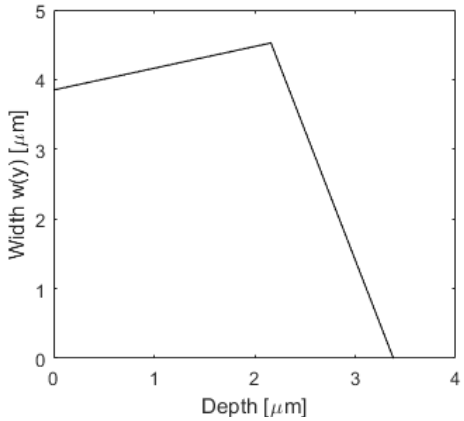

Figure 13. Width of the cantilever vs. depth as extracted from SEM frames for predicting the cantilever curvature.

These formulae were inserted into the following relations based on (2.2) and (2.3), taking into account the change of geometry and material properties with depth y:

$$F = \int_{y=0}^{1\cdot10^{-6}} \sigma(y') \cdot w(y')\, dy' + \int_{y=1\cdot10^{-6}}^{2.162\cdot10^{-6}} \sigma(y') \cdot w(y')\, dy' + \int_{y=2.162\cdot10^{-6}}^{3.38\cdot10^{-6}} \sigma(y') \cdot w(y')\, dy' = 0 \quad (3.3)$$

$$M = \int_{y=0}^{1\cdot10^{-6}} \sigma(y') \cdot w(y') \cdot y'\, dy' + \int_{y=1\cdot10^{-6}}^{2.162\cdot10^{-6}} \sigma(y') \cdot w(y') \cdot y'\, dy' + \int_{y=2.162\cdot10^{-6}}^{3.38\cdot10^{-6}} \sigma(y') \cdot w(y') \cdot y' dy' = 0 \quad (3.4)$$

This returns the linear system of equations

$$A = \begin{bmatrix} 2.13 & 2.86 \cdot 10^{-6} \\ 2.86 \cdot 10^{-6} & 5.38 \cdot 10^{-12} \end{bmatrix} \begin{bmatrix} a \\ b \end{bmatrix} = \begin{bmatrix} -0.00255 \\ -2.25 \cdot 10^{-9} \end{bmatrix},$$

The solution gives a = 0.0022 and b = -753.67±56m^{-1}.

10 References

[1] L.R. Brandt, E. Salvati, C. Papadaki, H. Zhang, S. Ying, E. Le Bourhis, I. Dolbnya, T. Sui, A.M. Korsunsky, Probing the deformation and fracture properties of Cu/W nano-multilayers by in situ SEM and synchrotron XRD strain microscopy, Surf. Coat. Technol. 320 (2017) 158–167. doi:10.1016/j.surfcoat.2017.01.065.

[2] C. Wang, P. Brault, C. Zaepffel, J. Thiault, A. Pineau, T. Sauvage, Deposition and structure of W-Cu multilayer coatings by magnetron sputtering, J. Phys. D. Appl. Phys. 36 (2003) 2709–2713. doi:10.1088/0022-3727/36/21/018.

[3] S. Djaziri, D. Thiaudière, G. Geandier, P.-O. Renault, E. Le Bourhis, P. Goudeau, O. Castelnau, D. Faurie, Controlled biaxial deformation of nanostructured W/Cu thin films studied by X-ray diffraction, Surf. Coatings Technol. 205 (2010) 1420–1425. doi:10.1016/j.surfcoat.2010.08.118.

[4] B. Girault, P. Villain, E. Le Bourhis, P. Goudeau, P.O. Renault, X-ray diffraction analysis of the structure and residual stresses of W/Cu multilayers, Surf. Coatings Technol. 201 (2006) 4372–4376. doi:10.1016/j.surfcoat.2006.08.034.

[5] B. Tlili, C. Nouveau, G. Guillemot, A. Besnard, A. Barkaoui, Investigation of the Effect of Residual Stress Gradient on the Wear Behavior of PVD Thin Films, J. Mater. Eng. Perform. 27 (2018) 457–470. doi:10.1007/s11665-018-3132-1.

[6] J.A. Thornton, J. Tabock, D.W. Hoffman, Internal stresses in metallic films deposited by cylindrical magnetron sputtering, Thin Solid Films. 64 (1979) 111–119. doi:10.1016/0040-6090(79)90550-9.

[7] A.M. Engwall, Z. Rao, E. Chason, Origins of residual stress in thin films: Interaction between microstructure and growth kinetics, Mater. Des. 110 (2016) 616–623. doi:10.1016/j.matdes.2016.07.089.

[8] G. Abadias, E. Chason, J. Keckes, M. Sebastiani, G.B. Thompson, E. Barthel, G.L. Doll, C.E. Murray, C.H. Stoessel, L. Martinu, Review Article: Stress in thin films and coatings: Current status, challenges, and prospects, J. Vac. Sci. Technol. A Vacuum, Surfaces, Film. 36 (2018) 020801. doi:10.1116/1.5011790.

[9] A.J. Lunt, N. Baimpas, E. Salvati, I.P. Dolbnya, T. Sui, S. Ying, H. Zhang, A.K. Kleppe, J. Dluhoš, A.M. Korsunsky, A state-of-the-art review of micron-scale spatially resolved residual stress analysis by FIB-DIC ring-core milling and other techniques, J. Strain Anal. Eng. Des. 50 (2015) 426–444. doi:10.1177/0309324715596700.

[10] R. Treml, D. Kozic, J. Zechner, X. Maeder, B. Sartory, H.-P. Gänser, R. Schöngrundner, J. Michler, R. Brunner, D. Kiener, High resolution determination of local residual stress gradients in single- and multilayer thin film systems, Acta Mater. 103 (2016) 616–623. doi:10.1016/j.actamat.2015.10.044.

[11] J. McCarthy, Z. Pei, M. Becker, D. Atteridge, FIB micromachined submicron thickness cantilevers for the study of thin film properties, Thin Solid Films. 358 (2000) 146–151. doi:10.1016/S0040-6090(99)00680-X.

[12] E. Salvati, A.M. Korsunsky, An analysis of macro- and micro-scale residual stresses of Type I, II and III using FIB-DIC micro-ring-core milling and crystal plasticity FE modelling, Int. J. Plast. 98 (2017) 123–138. doi:10.1016/j.ijplas.2017.07.004.

[13] M. Renzelli, M.Z. Mughal, M. Sebastiani, E. Bemporad, Design , fabrication and characterization of multilayer Cr-CrN thin coatings with tailored residual stress profiles, JMADE. 112 (2016) 162–171. doi:10.1016/j.matdes.2016.09.058.

[14] A.M. Korsunsky, E. Salvati, A.G.J. Lunt, T. Sui, M.Z. Mughal, R. Daniel, J. Keckes, E. Bemporad, M. Sebastiani, Nanoscale residual stress depth profiling by Focused Ion Beam milling and eigenstrain analysis, Mater. Des. 145 (2018) 55–64. doi:10.1016/j.matdes.2018.02.044.

[15] A. Zeilinger, J. Todt, C. Krywka, M. Müller, W. Ecker, B. Sartory, M. Meindlhumer,

M. Stefenelli, R. Daniel, C. Mitterer, J. Keckes, In-situ Observation of Cross-Sectional Microstructural Changes and Stress Distributions in Fracturing TiN Thin Film during Nanoindentation, Sci. Rep. 6 (2016) 1–14. doi:10.1038/srep22670.

[16] M. Stefenelli, J. Todt, A. Riedl, W. Ecker, T. Müller, R. Daniel, M. Burghammer, J. Keckes, X-ray analysis of residual stress gradients in TiN coatings by a Laplace space approach and cross-sectional nanodiffraction: a critical comparison, J. Appl. Crystallogr. 46 (2013) 1378–1385. doi:10.1107/S0021889813019535.

[17] U. Selvadurai, W. Tillmann, G. Fischer, T. Sprute, The influence of multilayer design on residual stress gradients in Ti/TiAlN systems, Mater. Sci. Forum. 768–769 (2014) 264–271. doi:10.4028/www.scientific.net/MSF.768-769.264.

[18] E. Chason, J.W. Shin, S.J. Hearne, L.B. Freund, Kinetic model for dependence of thin film stress on growth rate, temperature, and microstructure, J. Appl. Phys. 111 (2012). doi:10.1063/1.4704683.

[19] F.M. D'Heurle, J.M. Harper, Note on the origin of intrinsic stresses in films deposited via evaporation and sputtering, Thin Solid Films. 171 (1989) 81–92. doi:10.1016/0040-6090(89)90035-7.

[20] A.M. Korsunsky, A Teaching Essay on Residual Stresses and Eigenstrains, Butterworth-Heinemann, 2017.

[21] Q. Wang, S. Kishimoto, Y. Tanaka, K. Naito, Fabrication of nanoscale speckle using broad ion beam milling on polymers for deformation analysis, Theor. Appl. Mech. Lett. 6 (2016) 157–161. doi:10.1016/J.TAML.2016.07.001.

[22] E. Salvati, T. Sui, A.J.G. Lunt, A.M. Korsunsky, The effect of eigenstrain induced by ion beam damage on the apparent strain relief in FIB-DIC residual stress evaluation, Mater. Des. 92 (2016) 649–658. doi:10.1016/j.matdes.2015.12.015.

[23] E. Salvati, L.R. Brandt, C. Papadaki, H. Zhang, S.M. Mousavi, D. Wermeille, A.M. Korsunsky, Nanoscale structural damage due to focused ion beam milling of silicon with Ga ions, Mater. Lett. 213 (2018) 346–349. doi:10.1016/j.matlet.2017.11.043.

[24] A.M. Korsunsky, J. Guénolé, E. Salvati, T. Sui, M. Mousavi, A. Prakash, E. Bitzek, Quantifying eigenstrain distributions induced by focused ion beam damage in silicon, Mater. Lett. 185 (2016) 47–49. doi:10.1016/j.matlet.2016.08.111.

[25] J. Guénolé, A. Prakash, E. Bitzek, Influence of intrinsic strain on irradiation induced damage: the role of threshold displacement and surface binding energies, Mater. Des. 111 (2016) 405–413. doi:10.1016/j.matdes.2016.08.077.

[26] M. Senn, Digital Image Correlation and Tracking, (2015). https://uk.mathworks.com/matlabcentral/fileexchange/50995-digital-image-correlation-and-tracking.

[27] Material: Silicon (Si), bulk, (n.d.). https://www.memsnet.org/material/siliconsibulk/ (accessed October 19, 2018).

[28] A.M. Korsunsky, A Critical Discussion of the sin2ψ Stress Measurement Technique, Mater. Sci. Forum. 571–572 (2008) 219–224. doi:10.4028/www.scientific.net/MSF.571-572.219.

[29] I.C. Noyan, T.C. Huang, B.R. York, Residual stress/strain analysis in thin films by X-ray diffraction, Crit. Rev. Solid State Mater. Sci. 20 (1995) 125–177. doi:10.1080/10408439508243733.

[30] A. Benediktovich, I. Feranchuk, A. Ulyanenkov, Theoretical Concepts of X-Ray Nanoscale Analysis, 2014. doi:10.1007/978-3-642-38177-5.

[31] G.S. Schajer, ed., Practical Residual Stress Measurement Methods, John Wiley & Sons, Ltd, Chichester, UK, 2013. doi:10.1002/9781118402832.

[32] A.M. Korsunsky, S. Cherian, R. Raiteri, R. Berger, On the micromechanics of micro-cantilever sensors: Property analysis and eigenstrain modeling, Sensors Actuators, A Phys. 139 (2007) 70–77. doi:10.1016/j.sna.2007.03.007.